Journal of Marine Science and Application (2021) 20:646–659
https://doi.org/10.1007/s11804-021-00239-6

RESEARCH ARTICLE

Numerical Modeling of an Advanced Semi-SWATH Hull in Calm Water and Regular Head Wave

Arman Zare[1] · Hassan Sayyadi[1] · Mohammad Hossein Karimi[2]

Received: 27 November 2020 / Accepted: 07 October 2021 / Published online: 3 January 2022

Abstract

A small waterplane area twin hull (SWATH) has excellent seakeeping performance and low wave-making resistance, and it has been applied to small working craft, pleasure boats, and unmanned surface vehicles. However, with the increase in speed, the hydrodynamic resistance of SWATH will increase exponentially because of its large wet surface, followed by the uncomfortable situation of the hull underwater part relative to the water level and in terms of high trim by stern and high sinkage. A way to improve this situation is to reduce the depth of the draft at high speeds to ensure that all or a part of the volume of the submerged bodies is above the water level. Based on this idea, a new type of semi-SWATH hull form was analyzed in this paper. The two submerged bodies of the SWATH have a catamaran boat shape. This paper employed Siemens PLM Star-CCM+ to study the hydrodynamic performance of an advanced semi-SWATH model. Bare-hull resistance was estimated for both SWATH and CAT (CATAMARAN) modes in calm water. Moreover, the effect of fixed stabilizing fins with different angles on the vertical motions of the vessel in regular head waves was investigated with an overset mesh approach. The vertical motion responses were estimated at different wave encounter frequencies, and the present numerical method results have been verified by already published experimental data.

Keywords Seakeeping performance · Semi-SWATH · Stabilizing fins · Vertical motions · Overset mesh

1 Introduction

In recent years, improving the seakeeping performance has been one of the primary purposes of marine designers in the design of ships and floating structures. Environmental conditions during sea voyages of a ship can have a significant effect on the operability of marine vehicles.

Given that a small waterplane area twin hull (SWATH) hull has excellent seakeeping performance compared with the other conventional crafts, it has been used for different applications. In addition, numerical and experimental investigations have been carried out for the study and improvement of advanced SWATH hull performance in calm water and different wave conditions.

In addition to characteristics, such as the excellent seakeeping performance and low wave-making resistance of SWATH hull form, SWATHs are highly sensitive to weight distribution and dynamically unstable when the relative speed increases. As regards motion resistance, their performances are in the same range as conventional hull forms, except at extremely low relative speeds, at which the large wet surface worsens their performances. With regard to sea travels, the pitch

Article Highlights
- The numerical simulation of calm water performance for an advanced semi-SWATH hull at SWATH and CAT modes has been carried out by using CFD method and the weight fraction of each calm water resistance components was studied.
- The grid uncertainty study of CFD method for semi-SWATH hulls is studied.
- The effectiveness of fixed stabilizing fins, for control and reduction of semi-SWATH vertical motions under regular head wave, is studied.
- The numerical simulation of seakeeping performances for semi-SWATH hull has been carried out (in regular head wave and at different Froude numbers) and RAO diagrams for heave, pitch, and vertical acceleration were depicted.

✉ Mohammad Hossein Karimi
mhkcom480@yahoo.com

[1] Department of Mechanical Engineering, Sharif University of Technology, Tehran 11155-9567, Iran

[2] Department of Mechanical and Aerospace Engineering, Malek-Ashtar University of Technology, Esfahan 1774-15875, Iran

response is of particular concern because, notably, large encounter periods that are close to the pitch resonance are likely to occur over a wide range of wavelengths. With the increase in speed, the hydrodynamic resistance of SWATH will increase exponentially because of its large wet surface, followed by the uncomfortable situation of the hull underwater part relative to the water level and in terms of high trim by stern and high sinkage. A way to improve this situation is to reduce the depth of the draft at high speeds to ensure that all or a part of the volume of submerged bodies is above the water level. Based on this idea, several new types of semi-SWATH hull forms have been developed. In addition, based on the design purposes of crafts and their specific missions, different types of HYBRID SWATH hull were designed and studied for the improvement of standard SWATH hull form performance at high speeds in calm water and rough seas. Most designs concern the replacement of standard SWATH submerged bodies with a catamaran, planing, and other hull shapes to cope with the natural disadvantages of the SWATH hull form. In SWATH-CAT hull form, the two submerged bodies of the SWATH have a catamaran shape. Therefore, at a low draft, the SWATH-CAT behaves as a catamaran, and at higher drafts, the SWATH mode will be used. Based on the different modes of operation (SWATH or CAT mode), the vessel has different performances, and this flexibility in features compared with standard SWATH or catamaran hull forms will give interesting characteristics for most of SWATH application fields (Dubrovsky and Lyakhovitsky 2001; Dubrovsky et al. 2007). The standard SWATH hull form also has numerous applications in offshore industries. The buoyancy force is provided by two torpedo-like submerged hulls below the water level. Struts connect the lower hulls to the transverse structures above the water level. The struts have a small waterplane area, consequently making the vessel less sensitive to the wave impacts compared with other conventional vessels, such as mono-hulls and catamarans (Gupta and Schmidt 1986).

In 2001, a new catamaran hull form was developed by BMT Nigel Gee in the UK, which led to the semi-SWATH (CAT mode) hull form technology. In this new technology, the waterplane is more constricted, and the height of the center of buoyancy has lower values. Moreover, the bulbous bow has a slender shape (Yun et al. 2018). The semi-SWATH technology fills the gaps in the hydrodynamics performance between the catamaran and SWATH. Hence, the motion-seasickness incidence and motion-induced interruptions of the semi-SWATH decrease compared with those of the catamaran. Conversely, the SWATH requires a significant power in comparison with the semi-SWATH (Jupp et al. 2014). In other words, the semi-SWATH technology is essentially an attempt to show the benefits of the catamaran and SWATH and to avoid their drawbacks.

The first research about numerical optimization of SWATH hull form was carried out by Salvesen et al. (1985), who presented and developed a computational method for wave resistance minimization. Chan (1993) investigated the motion and dynamic structural responses of antisubmarine rescue catamaran and 3000-ton SWATH by a 3D linearized potential theory related to a cross-flow method with consideration of viscous effects. Campana and Peri (2000) introduced a new hull form with a medium waterplane area called MWATH by reforming the strut shape and underwater gondolas of a SWATH hull. Guttenplan (2007) studied the performance of a prototype 10000 kg reduced waterplane area twin hull, including the effect of variable demi-hull separation on the resistance in calm water and quasi-active foil control on the motion responses in waves by Rankine panel numerical method using SWAN2 2002 software package. Brizzolara et al. (2015) studied the hydrodynamic performance of unconventional SWATH and semi-SWATH with numerical methods. In their research, the resistance force in calm water was calculated using the boundary element method (BEM) combined with viscous effects and multiphase unsteady Reynolds-averaged Navier-Stokes equation (URANSE) solver. Heave and pitch responses of two hull forms were also obtained in regular head wave conditions by a frequency domain 3D panel method. Begovic et al. (2015) provided a detailed report on the computational fluid dynamics (CFD) numerical method for the hydrodynamic assessment of the SWATH concept; their study was conducted in CD Adapco Star-CCM+ using the overset mesh approach. For a semi-SWATH hull form, the influence of stabilizing fins on the resistance in calm water has been experimentally carried out by Ali et al. (2015). The semi-SWATH model was tested with fixed fore fins at 0° and aft fin angle adjustable to 0°, 5°, and 15° at the range of Froude numbers from 0.34 to 0.69. Their evaluations showed that the fluid flow around the hull at different speeds was under the influence of the fin angle, and this dependence varied based on the Froude number. Vernengo and Bruzzone (2016) studied and compared the calm water resistance and seakeeping quality of a new semi-SWATH design and a classical single-strut SWATH hull using the numerical BEM developed by Bruzzone (1994, 2003). Furthermore, the authors investigated the effect of passive stabilizing fins on heave and pitch responses of a full-scale conventional SWATH hull, which has been experimentally tested by Kallio (1976). Wang et al. (2016), by presenting a SWATH planing unmanned surface vessel and using the CFD method, numerically simulated this vessel at various velocities and showed that given the reduction of the wetted surface and the production of the desired lift force, the resistance can be significantly reduced at high speeds. Sun et al. (2016) investigated the seakeeping performance of a slender catamaran with a semisubmerged bow using the CFD method. In this study, based on the overset mesh and motion region techniques, motion responses of the vessel in regular head waves were estimated at various wavelengths and speeds. They showed that the overset mesh technique is precise in predicting motions. Vernengo and Brizzolara (2017), based on previous studies about SWATH optimization (Brizzolara and Vernengo 2011), presented a systematic evaluation of the influence of various forms and canting angles of

struts. Vernengo et al. (2018) evaluated the motion responses of three hull forms, including SWATH, catamaran, and trimaran, by applying a first-order 3D BEM. Bonfiglio et al. (2018) studied the seakeeping performance of SWATH design using multifidelity Gaussian process regression and Bayesian optimization. Their studies indicated the excellent features of this optimization framework in modeling and identifying optimal alternative designs with a remarkable reduction in computational costs. Begovic et al. (2019) performed a broad experimental study on four different SWATH model hull forms in calm water and regular and irregular waves. The scope of their research was the calculation of resistance in calm water and heave, pitch, and vertical acceleration RAO diagrams in waves. Pérez-Arribas and Calderon-Sanchez (2020) introduced a method based on a parametric computer to design a B-spline model of a SWATH hull with the use of Chebyshev functions. In this new technique, variables, including displacement (Δ), waterplane area (A_{wp}), center of buoyancy, and center of flotation, can be controlled.

In this paper, the CFD numerical method by Siemens PLM Star-CCM+ was used to predict resistance force in calm water and simulation of vertical motions in regular head waves for an advanced semi-SWATH model. In calm water, the total resistance for SWATH and CAT modes was calculated and compared with available experimental data. The effect of fixed stabilizing fins on the reduction of heave and pitch motions in regular head wave conditions for a specific encounter frequency was also investigated, and the semi-SWATH bare-hull vertical motions in regular head waves, including heave, pitch, and vertical acceleration RAO, were estimated at four different Froude numbers and wide wave frequency range.

2 Main Characteristics of Semi-SWATH Hull Form and Fixed Stabilizing Fins

Table 1 shows the main particulars of the semi-SWATH model used in the present study. The selected hull form model for the present study was based on Yaakob and Mekanikal (2006) experimental investigation; the same model has been used. Table 2 provides the main particulars of the stabilizing fins. Figure 1 shows the semi-SWATH model equipped with stabilizing fins.

Table 1 Main particulars of the semi-SWATH model (Yaakob and Mekanikal 2006)

Properties	Value
Length of the main hull (m)	2.31
Maximum beam (m)	0.80
Draft (SWATH mode) (m)	0.20
Draft (CAT mode) (m)	0.14
Displacement (SWATH mode) (kg)	76.877
Displacement (CAT mode) (kg)	53.176
Radius of gyration for pitch (m)	0.578
Longitudinal center of gravity abaft midships (m)	0.089
Maximum speed (m/s)	3.25

Table 2 Main particulars of stabilizing fins (Yaakob and Mekanikal 2006)

Properties	Fore fin	Aft fin
Chord (m)	0.096	0.145
Span (m)	0.120	0.186
Longitudinal location[1] (m)	1.95	0.35
Vertical location[2] for SWATH mode (m)	0.151	0.151
Vertical location[2] for CAT mode (m)	0.092	0.092
Maximum thickness (m)	0.015	0.023
Fin type	NACA–0015	

[1]Distance from the main hull stem to the fin quarter–chord point

[2]Distance from the water level to the chord line

3 Numerical Simulation Procedures Description (Physical Setup, Modeling, and Grid Uncertainty Analysis)

3.1 Governing Equations and Numerical Simulation Setup

In this paper, simulations were carried out using the finite volume method for the solution of URANSE (Ferziger and Perić 2002):

$$\begin{aligned}
&\frac{\partial(\rho\overline{u}_i)}{\partial x_i} = 0\\
&\frac{\partial(\rho\overline{u}_i)}{\partial t} + \frac{\partial}{\partial x_j}\left(\rho\overline{u}_i\overline{u}_j + \rho\overline{u_i'u_j'}\right) = -\frac{\partial\overline{p}}{\partial x_i} + \frac{\partial\overline{\tau}_{ij}}{\partial x_j}\\
&\frac{\partial\alpha}{\partial t} + \overline{u}_i\frac{\partial\alpha}{\partial x_i} = 0
\end{aligned} \tag{1}$$

The governing equations include the continuity, momentum, and volume fraction transport equations for incompressible flows. Here, $\overline{\tau}_{ij}$ is the mean viscous stress tensor component:

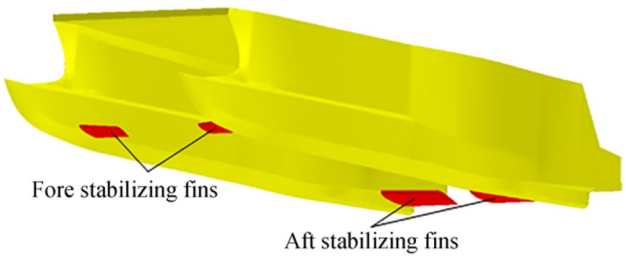

Figure 1 Semi-SWATH model equipped with stabilizing fins

Table 3 Numerical simulation setup summary

Parameter	Settings
Turbulence model	Standard k–ε
Continuity and momentum equation coupling	SIMPLE - Algorithm
Method	Segregated flow
Solver	3D, implicit unsteady
Multiphase model	VOF
Time step	Equations (5) and (6)
Time discretization	First order
Convection scheme for VoF	HRIC
Iterations per time step	10

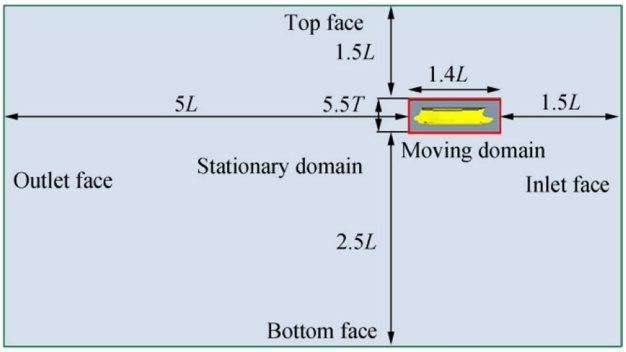

Figure 2 Dimensions of the computational domain. The width of background and overset are 2L and 3B, respectively

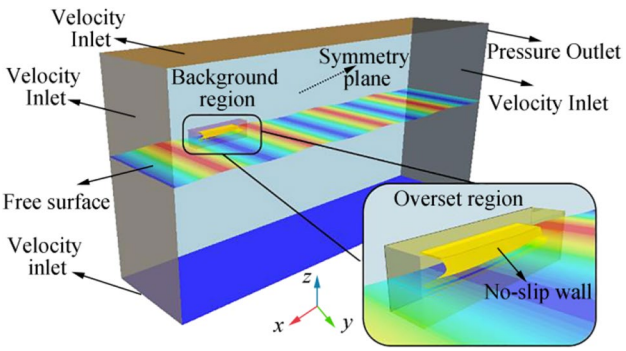

Figure 3 General view of the computational domain with boundary conditions

$$\overline{\tau}_{ij} = \mu\left(\frac{\partial \overline{u}_i}{\partial x_j} + \frac{\partial \overline{u}_j}{\partial x_i}\right) \tag{2}$$

Variable ρ is the mixture density, $\overline{u}_i$ is the averaged Cartesian components of the velocity vector in the x_i direction ($i, j = 1, 2, 3$), $\rho\overline{u_i' u_j'}$ is the Reynolds stress, $\overline{p}$ is the mean pressure field, μ is the dynamic viscosity, and (α) represents the volume fraction of water inside each cell.

The component of $\rho\overline{u_i' u_j'}$ was obtained based on the Boussinesq approximation by the k–ε turbulence model selected for this simulation:

$$\begin{aligned}\frac{\partial(k)}{\partial t} + \frac{\partial(\overline{u}_j k)}{\partial x_j} &= \frac{\partial}{\partial x_j}\left[\left(\nu + \frac{\nu_t}{\sigma_k}\right)\frac{\partial k}{\partial x_i}\right] + P_k - \varepsilon \\ \frac{\partial(\varepsilon)}{\partial t} + \frac{\partial(\overline{u}_j \varepsilon)}{\partial x_j} &= \frac{\varepsilon}{k}\left(C_{\varepsilon 1} P_k - \rho C_{\varepsilon 2}\varepsilon\right) + \frac{\partial}{\partial x_j}\left[\left(\nu + \frac{\nu_t}{\sigma_\varepsilon}\right)\frac{\partial \varepsilon}{\partial x_j}\right]\end{aligned} \tag{3}$$

where $\nu_t = C_\mu k^2/\varepsilon$ is the eddy viscosity; k is the turbulent kinetic energy; ε is the dissipation term of turbulent kinetic energy; P_k is the production of turbulent kinetic energy; and $C_\mu = 0.9$, $C_{\varepsilon 1} = 1.44$, $C_{\varepsilon 2} = 1.92$, $\sigma_k = 1.0$, $\sigma_\varepsilon = 1.3$ are model constants.

Frisk and Tegehall (2015) noted that the standard k–ε model is robust and gives accurate results for free surface simulations for completely turbulent flows. Table 3 summarizes the numerical simulation setup summary. The volume of fluid (VOF) method was employed with high-resolution interface capturing (HRIC). The primary application of the implicit unsteady solver is the detection and management of the region of all unknown hydrodynamic values with an iterative solver for each time step. Only the unsteady solver can be combined with the segregated flow model (Voxakis 2012). A minimum of 10 inner iterations for each time step was used.

The convective Courant number (CFL) relates the time step (Δt) to the grid flow velocity (U) and the cell size dimension (Δx) as follows:

$$\mathrm{CFL} = U\frac{\Delta t}{\Delta x} \tag{4}$$

In general, the CFL should be less than or equal to 1 to achieve the desired results and stability of the numerical solution. Reducing this value gives numerical solution stability despite the increase in computational cost.

In implicit unsteady simulations, the time step value was obtained based on the flow properties. Therefore, the time step employed in the calm water condition, as a function of vessel speed (V) and length between perpendiculars (L), was determined in accordance with the ITTC (2011):

$$\Delta t_{\text{Calm water}} = 0.005 - 0.01\frac{L}{V} \tag{5}$$

Table 4 Location of computational domain faces in similar previous works

Reference	Inlet face	Outlet face	Top face	Bottom face	Side face
Tezdogan et al. (2015)	1.15L	4.5L	L	2.3L	2.5L
Sun et al. (2016)	1.5L	3L	L	2L	L
Kahramanoğlu et al. (2020)	2.75L	7.75L	0.9L	1.9L	3L

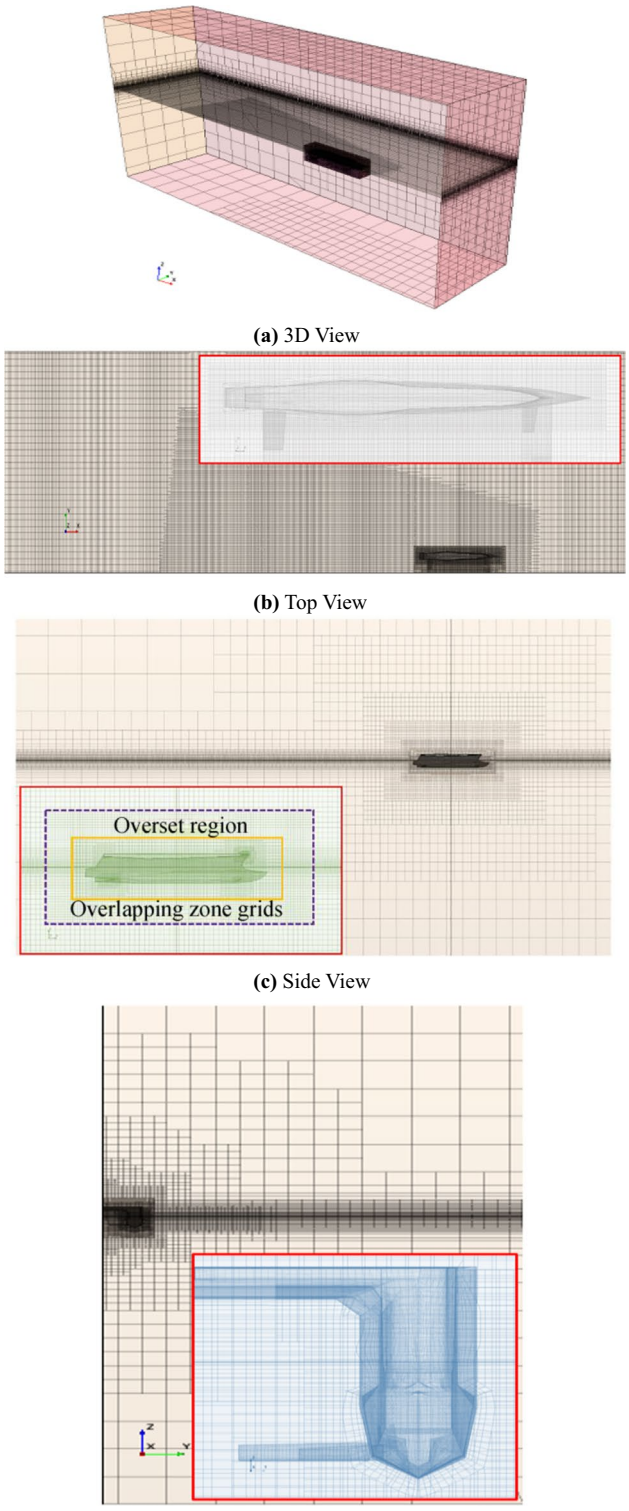

(a) 3D View

(b) Top View

(c) Side View

(d) Front View

Figure 4 Views of grid generation in the computational domain. **a** 3D view. **b** Top view. **c** Side view. **d** Front view

In wave condition simulation, at least 100 time steps for each wave encounter period (T_e) were utilized, as suggested by ITTC (2011) and another relevant study (Tezdogan et al. 2015). Therefore, for this condition, the time step size was computed as follows:

$$\Delta t_{\text{Wave}} = \frac{T_e}{100} \tag{6}$$

3.2 Computational Domain and Boundary Conditions

Figures 2 and 3 illustrate the computational domain dimensions and applied boundary conditions, respectively. The domain dimensions must be large enough to achieve high precision and reliable numerical results. In Figure 2, L, B, and T

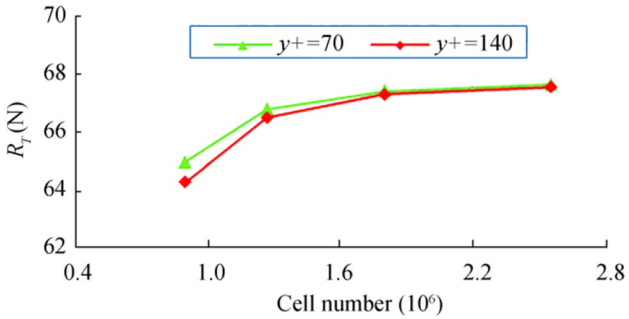

Figure 5 Grid independence analysis for total resistance prediction in calm water at $Fr=0.68$

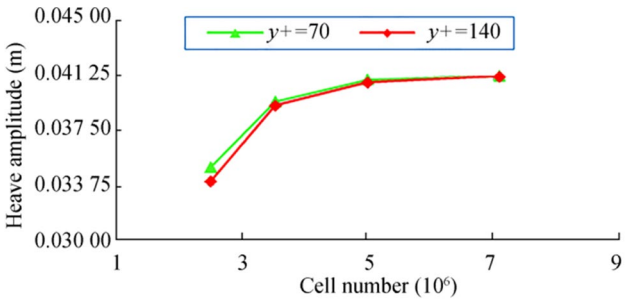

(a) Heave motion

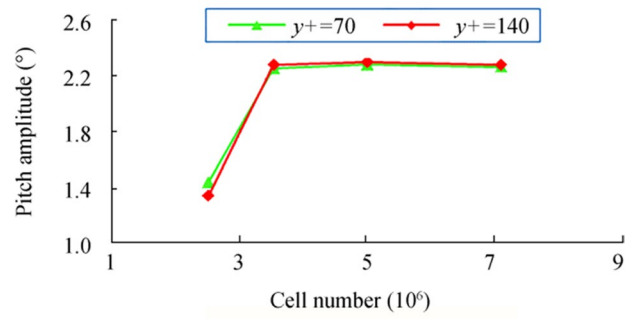

(b) Pitch motion

Figure 6 Grid independence analysis in wave condition with length $\lambda_w/L=1.8$ at $Fr=0.512$

Table 5 Number of cells for calm water and wave condition simulations

Simulation	Region		
	Background	Overset	Total
Calm water	1.80×10^6	–	1.80×10^6
Wave condition	1.35×10^6	2.18×10^6	3.53×10^6

are the length between perpendiculars, half beam, and draft of the vessel, respectively. For simulations of free surface with incident waves, the computational domain is extended $1.5L$ upstream of the hull, which is defined as an inlet face, and $5L$ downstream, which is considered an outlet face, to avoid any wave reflections according to the ITTC (2011) recommendations. Similar previous works were also studied to set up the appropriate location of computational domain faces (Table 4). Given the symmetry, only half of the model hull was modeled. Therefore, the symmetry plane condition of the longitudinal centerline was considered. Other boundary conditions were defined as follows. The inlet, side, top, and bottom faces were set to velocity inlet as a field function of volume fraction and velocity. The outlet face was imposed on the pressure outlet as a field function of volume fraction and pressure. The vessel hull surface was defined as a no-slip wall condition.

In calm water, the computational domain includes the stationary domain only, and the vessel is fixed to heave and pitch. Given that only the resistance force prediction is targeted, for the simulation in wave conditions, the computational domain was specified in two regions to predict vessel responses, including background (stationary domain) and overset (moving domain) regions. Therefore, during the simulation in wave conditions, the vessel was free to heave and pitch motions and move with the overset region at each time step. For this purpose, a setting called dynamic fluid body interaction was employed to simulate the interactions between the fluid and rigid body.

A linear interpolation approach was employed to control the numerical data transfer between the two regions. In the overset method, no specific recommendation concerns the size of the overset region dimensions. However, dimensions with a sufficient number of cells between the surface boundary of the vessel hull inside the overset and background regions are acceptable.

Table 6 GCI estimation-related parameters (Celik et al. 2008)

Parameter	Definition
$\varphi_{\text{ext}}^{BC} = \frac{r_{BC}^{P}\varphi_C - \varphi_B}{r_{BC}^{P}-1}$	Extrapolated value
$e_a^{BC} = \left\lvert \frac{\varphi_C - \varphi_B}{\varphi_C} \right\rvert$	Approximate relative error
$e_{\text{ext}}^{BC} = \left\lvert \frac{\varphi_{ext}^{CB} - \varphi_C}{\varphi_{ext}^{CB}} \right\rvert$	Extrapolated relative error
$\text{GCI}_{\text{Fine}}^{BC} = \frac{1.25e_a^{BC}}{r_{BC}^{P}-1}$	Fine-grid convergence index

3.3 Grid Generation

The grid division was performed using the automated mesh technique in the Siemens PLM Star-CCM+ package. Both simulation conditions (calm water and wave) were accomplished with an unstructured hexahedral cell (trimmed) mesher, which is suitable for solving complex problems, especially at the free surface. The mesh generation process was conducted based on dimensions, including the total thickness of prism layers and maximum and minimum sizes of grid cells in the desired areas (surface and volume controls), especially around the hull surface with fins and the free surface area as a percentage of base size.

When employing the overset mesh approach, a refinement area called the "overlapping zone," where the numerical data are exchanged between the stationary and moving domains through the overlapping zone grids, must be used. Siemens PLM Star-CCM+ user guide (Siemens 2019) provided suggestions on how to set appropriate grid cells in the overlapping zone. Figure 4 depicts the 3D, top, side, and front views of grid division in the computational domain.

3.3.1 Grid Independence Analysis

A grid independence analysis is an essential issue for numerical simulations. All the physical phenomena related to flow around the vessel must be modeled with the desired quality. Therefore, the sensitivity of the numerical results concerning cell number and dimensionless wall distance ($y+=u^*y/v$, where u^* is the friction velocity, y is the absolute distance from the nearest

Table 7 Grid uncertainty study for total resistance in calm water

Parameter	Calm water ($Fr=0.68$)	
	Case of A-B-C	Case of B-C-D
r_{BC}, r_{AB}	$\sqrt{2}$	$\sqrt{2}$
φ_A	65.00	66.80
φ_B	66.80	67.42
φ_C	67.42	67.63
R	0.3444	0.3387
p	3.0753	3.1237
$\varphi_{\text{ext}}^{BC}$	67.7457	67.7375
e_{ext}^{BC}	0.4831%	0.1590%
e_a^{BC}	0.9196%	0.3105%
$\text{GCI}_{\text{Fine}}^{BC}$	0.6040%	0.1988%

Table 8 Grid uncertainty study for heave and pitch amplitudes in regular head wave

Parameter	Wave condition ($\lambda_w/L=1.8$, $Fr=0.512$)			
	Case of A′-B′-C′		Case of B′-C′-D′	
	Heave (m)	Pitch (°)	Heave (m)	Pitch (°)
r_{BC}, r_{AB}	$\sqrt{2}$	$\sqrt{2}$	$\sqrt{2}$	$\sqrt{2}$
$\varphi_{A'}$	0.0350	1.450	0.0395	2.273
$\varphi_{B'}$	0.0395	2.273	0.0410	2.310
$\varphi_{C'}$	0.0410	2.310	0.0412	2.285
R	0.3333	0.0449	0.1333	−0.67
p	3.1699	8.9506	5.8138	1.1311
$\varphi_{\text{ext}}^{B'C'}$	0.0417	2.3117	0.0412	2.2329
$e_{\text{ext}}^{B'C'}$	1.8292%	0.0754%	0.0747%	2.2793%
$e_{a}^{B'C'}$	3.6585%	1.6017%	0.4854%	1.0941%
$\text{GCI}_{\text{Fine}}^{B'C'}$	2.2865%	0.0942%	0.0933%	2.8492%

wall, and v is the kinematic viscosity) for proper turbulence modeling should be investigated. For this purpose, four types of cell numbers, namely, 0.9×10^6 (A-type), 1.27×10^6 (B-type), 1.8×10^6 (C-type), and 2.55×10^6 (D-type), were selected for the simulation in calm water, and another four types, such as 2.50×10^6 (A′-type), 3.53×10^6 (B′-type), 5.0×10^6 (C′-type), and 7.1×10^6 (D′-type), were used for wave conditions. A high-y+ treatment model was employed to keep the low numbers of grid cells. In this particular approach, near-wall y+ was kept at a value higher than 30 as recommended by Siemens PLM Star-CCM+ user guide (Siemens 2019). A good range was between 60 and 130, as reported by Cucinotta et al. (2018). Figures 5 and 6 show the numerical results in calm water (total resistance) and wave (heave and pitch amplitudes), respectively, for the bare-hull as a function of cell number for two different values of y+ approximately 70 and 140. The cell numbers of 1.8×10^6 and 3.53×10^6 with y+ of 70 were selected for the simulation in calm water and wave conditions, respectively. Table 5 contains the number of cells in both overset and background regions for each simulation.

3.3.2 Grid Uncertainty Estimation

The grid (U_G), time step (U_{TS}), and iterative (U_I) uncertainties are the main sources of numerical uncertainty (U_{SN}):

$$U_{\text{SN}}{}^2 = U_G{}^2 + U_{\text{TS}}{}^2 + U_I{}^2 \tag{7}$$

Among the main sources of numerical uncertainties mentioned above, grid uncertainty has the greatest impact, as reported by Wilson et al. (2001) and De Luca et al. (2016).

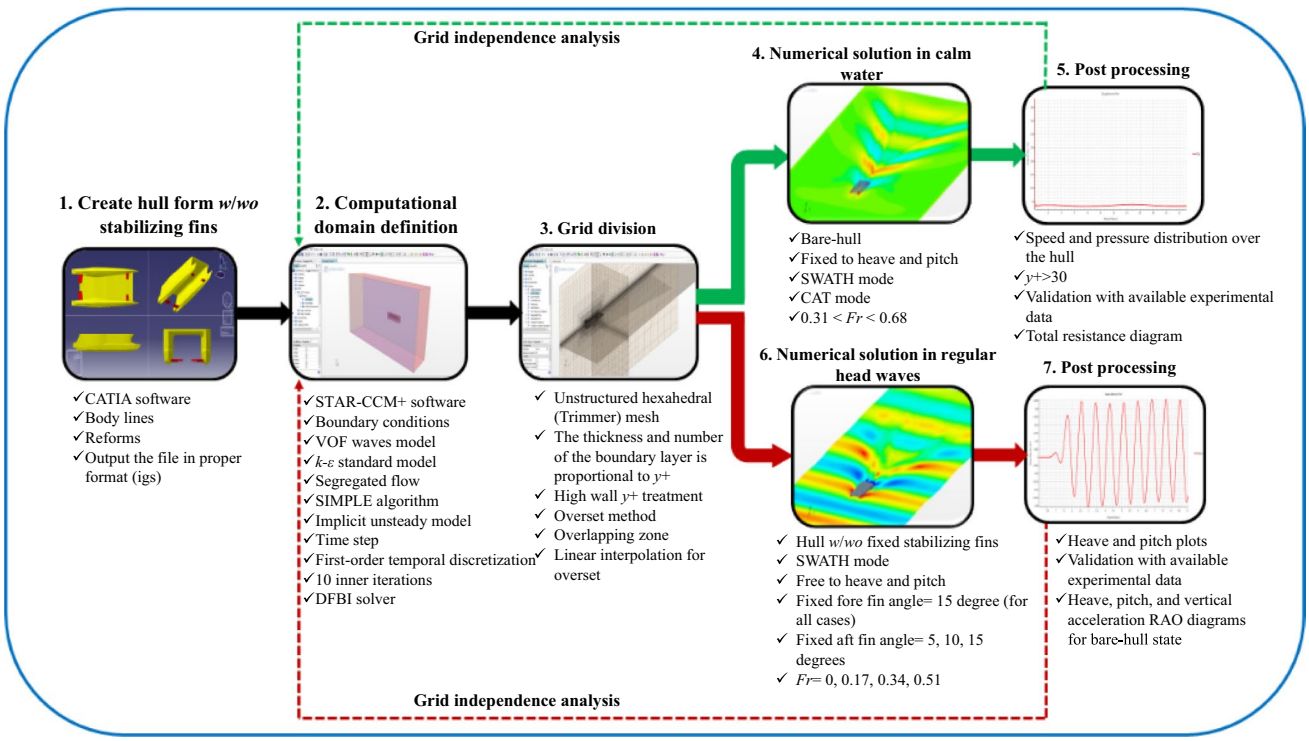

Figure 7 Numerical simulation steps of the semi-SWATH model

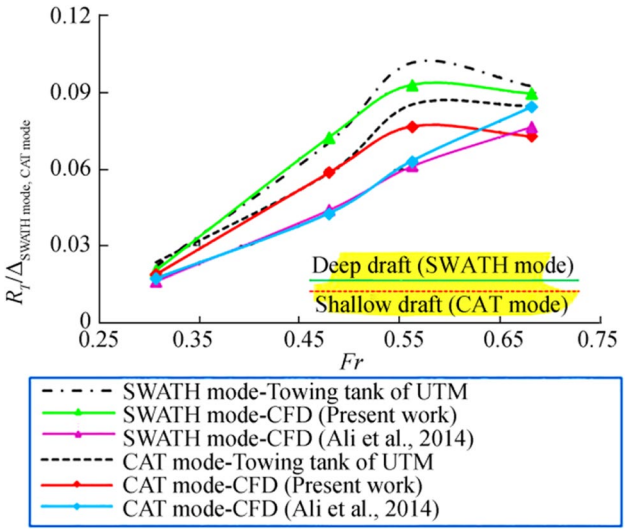

Figure 8 Computed resistance–weight ratio using the CFD method (present work and Ali et al. (2014)) in comparison with available experimental data at different Froude numbers from 0.31 to 0.68

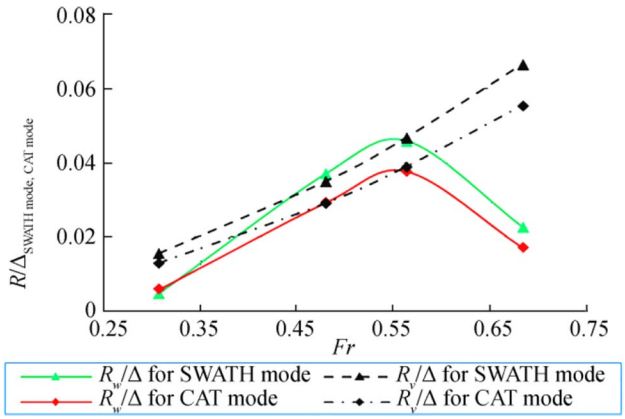

Figure 9 Comparison of estimated wave and viscous resistance for CAT and SWATH modes at different Froude numbers from 0.31 to 0.68

Special attention unless commonly used in your field, we suggest providing the meaning of acronyms at first mention in both abstract and main text. However, acronyms are not included when terms are mentioned only once in the paper. For this purpose, the difference between any solution scalars (ε) can be computed as follows:

$$\varepsilon_{BC} = \varphi_B - \varphi_C, \quad \varepsilon_{AB} = \varphi_A - \varphi_B \tag{8}$$

where φ_A, φ_B, and φ_C refer to the value of any scalar of coarse, medium, and fine-grid size, respectively. The convergence ratio was utilized to evaluate the convergence condition (R), as given in Eq. (9):

$$R = \frac{\varepsilon_{BC}}{\varepsilon_{AB}} \tag{9}$$

According to the ITTC (2002) guidelines and Stern et al. (2006), three convergence conditions are defined as follows:

$$\begin{cases} \text{Monotonic convergence}: & 0 < R < 1 \\ \text{Oscillatory convergence}: & -1 < R < 0 \\ \text{Divergence}: & R < -1, R > 1 \end{cases} \tag{10}$$

The apparent order (p) can be obtained as follows (Celik et al. 2008):

$$\begin{aligned} p &= \frac{1}{\ln r_{BC}} \left| \ln \left| \varepsilon_{AB}/\varepsilon_{BC} \right| + q(p) \right| \\ q(p) &= \ln \left(\frac{r_{BC}^{p} - s}{r_{AB}^{p} - s} \right) \\ s &= \text{sign}\ \left(\varepsilon_{AB}/\varepsilon_{BC} \right) \end{aligned} \tag{11}$$

Table 6 presents the other terms related to the GCI estimation, including the extrapolated value, approximate relative error, extrapolated relative error, and fine-grid convergence index (Celik et al. 2008).

Tables 7 and 8 present the uncertainties of calm water total resistance and heave and pitch amplitudes in regular head wave conditions for the semi-SWATH model, respectively. As shown in Table 7, in both A-B-C and B-C-D cases, the total resistance converged monotonically. In Table 8, the grid uncertainty study showed monotonic convergence for both heave and pitch amplitudes in the case of A′-B′-C′, whereas for the case of B′-C′-D′, the

Table 9 Comparison of the CFD results of the present work and available experimental data

Fr	Total resistance–weight ratio (R_T/Δ)					
	CAT mode			SWATH mode		
	Present work	Towing tank of UTM	Error (%)	Present work	Towing tank of UTM	Error (%)
0.31	0.022	0.023	−4.35	0.021	0.022	−4.54
0.48	0.059	0.058	1.72	0.072	0.070	2.86
0.56	0.077	0.085	−9.41	0.094	0.101	−6.93
0.68	0.073	0.084	−13.10	0.089	0.092	−3.26

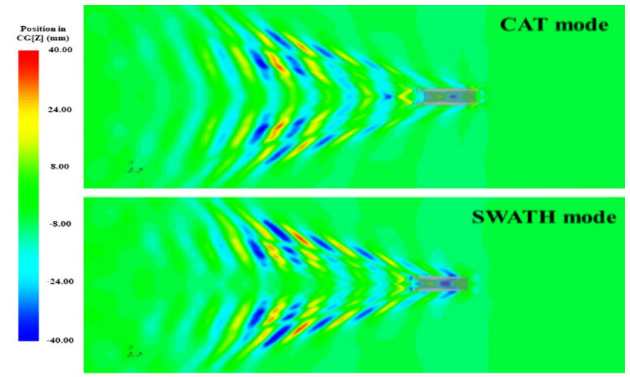

(a) $Fr = 0.31$

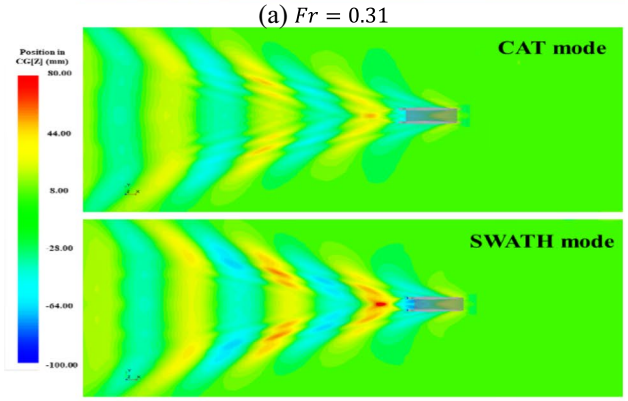

(b) $Fr = 0.48$

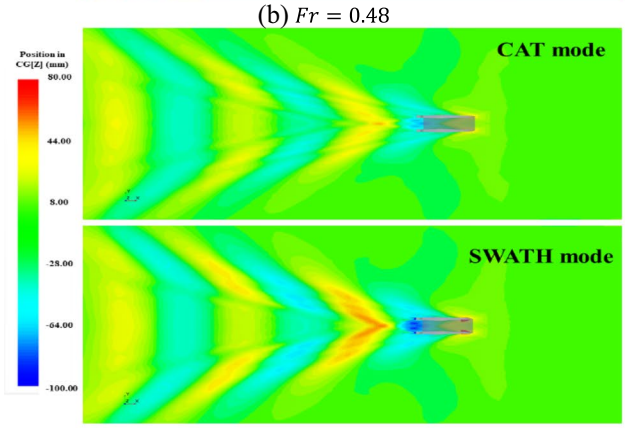

(c) $Fr = 0.56$

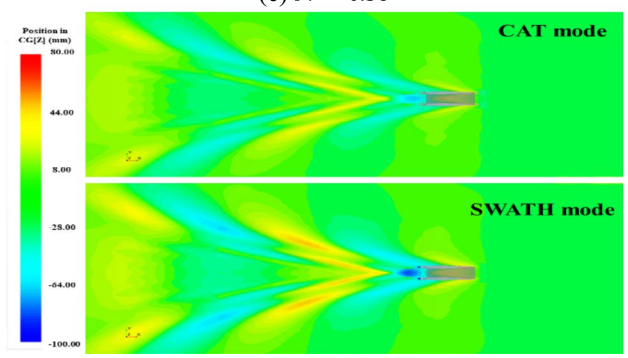

(d) $Fr = 0.68$

Figure 10 Comparison of wave pattern induced by the semi-SWATH motion at SWATH and CATs mode in calm water at Froude numbers from 0.31 to 0.68

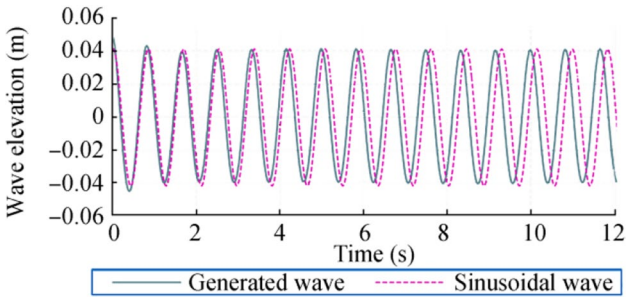

Figure 11 Comparison of the time history of wave elevation by numerical wave probe and sinusoidal wave (wave condition with length $\lambda_w/L = 1.8$ and steepness $h_w/\lambda_w = 0.02$ at $Fr = 0.512$)

pitch amplitude displays oscillatory convergence. After the GCI method assessment, the CFD simulations in calm water and wave conditions were carried out with C- and B′-type grids, respectively.

4 Performance Evaluation in Calm Water and Regular Head Waves

Figure 7 illustrates the numerical simulation steps of the semi-SWATH model in calm water and wave conditions at a glance.

4.1 Resistance in Calm Water

The total resistance coefficient (C_T) for multihull vessels can be written as follows:

$$C_T = \tau C_W + (1 + \beta k) C_f \tag{12}$$

where k is the form factor, which was assumed similar for the single and multihull analyses. τ is the wave resistance interference factor. β is the viscous resistance interference factor.

As shown in Figure 8, the total resistance–weight ratio (R_T/Δ) of the present work was compared with the numerical results from Ali et al. (2014) research and available experimental data for the semi-SWATH model in SWATH and CAT modes. The available experimental data were measured in a towing tank at the Marine Technology Center of Universiti Teknologi Malaysia (UTM), as reported by Ali et al. (2014).

Table 9 shows the percentage of error between the CFD results of the present work and the available experimental data at different Froude numbers from 0.31 to 0.68.

Figure 8 shows that the presented CFD results are in good correlation with the experimental data compared with the CFD results of Ali et al. (2014) due to the high quality of generated grid cells on the hull surfaces and control volumes in

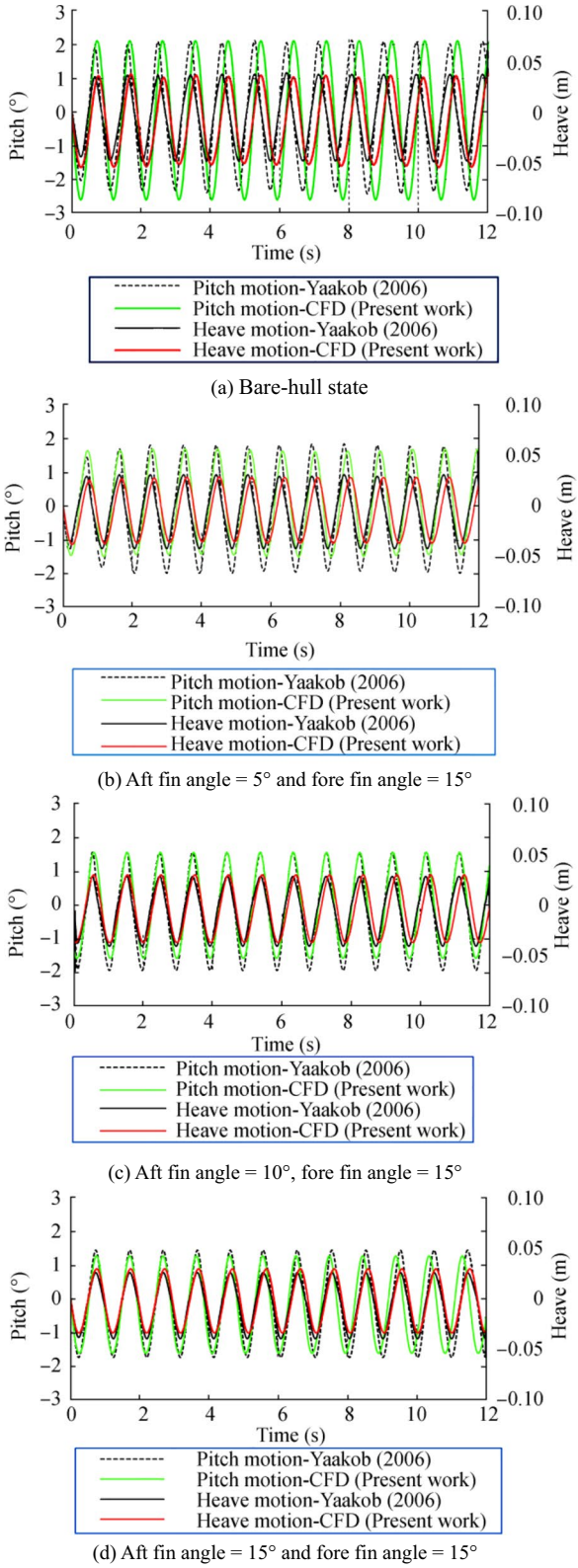

Figure 12 Heave and pitch motions of the semi-SWATH vessel with and without fixed stabilizing fins at the wavelength $\lambda_w/L=1.8$ and wave steepness $h_w/\lambda_w=0.02$

Table 10 Vertical motion reduction

Fore fin angle (°)	Aft fin angle (°)	Heave motion reduction (%)	Pitch motion reduction (%)
15	5	20.32	16.98
15	10	34.54	23.18
15	15	32.08	35.17

the required wake areas. At $Fr>0.56$, the presented numerical method underestimated the total resistance–weight ratio for SWATH and CAT modes. The maximum error between the results of the present work and experimental data approximated 6.93% and 13.10% (Table 9) for the SWATH and CAT modes, respectively. The main reason for the relatively high discrepancies of the results at $Fr > 0.56$ can be the fixed heave and pitch motions of the vessel in numerical simulations of the present work. In general, the comparison of the total resistance–weight ratio of SWATH and CAT modes indicated the advantages of the semi-SWATH hull with respect to the standard SWATH hull form.

The curves (dashed and dot-dash) estimated in Figure 9 indicate that the vessel at SWATH mode has higher viscous resistance (R_v) than the CAT mode due to the higher wetted surface. Figure 9 shows that the wave resistance (R_w) for CAT and SWATH modes at the Froude number of 0.56 peaked and then reduced. Figure 10a, b, c, and d show the cross-comparison of wave pattern predicted by the CFD method in calm water for SWATH and CAT modes at Froude numbers from 0.31 to 0.68. Figure 10 demonstrates that the vessel at SWATH mode generated waves with relatively large peaks and troughs with respect to the CAT mode on the inner and outer sides of the struts for different velocities, consistent with the finding in Figure 9 (green and red curves). Therefore, the main reason for total resistance reduction of the vessel for the SWATH and CAT modes at $Fr>0.56$ (as depicted in Figure 8) was the reduction of wave resistance, which is consistent with the findings of Brizzolara et al. (2015).

4.2 Motion in Wave

In this section, heave and pitch motions of the semi-SWATH model with and without fixed stabilizing fins were obtained. First, simulations were carried out based on Yaakob and Mekanikal (2006) experimental test on regular head wave conditions with wavelength $\lambda_w/L=1.8$ and wave steepness $h_w/\lambda_w=0.02$ at a Froude number of 0.512. The fore fin angle was fixed at 15°, whereas the aft fin angle was varied to 5°, 10°, and 15° in accordance with the work of Yaakob and Mekanikal (2006). The stall effect (lift breakdown) occurred at more than 0.4 rad (23°) for the NACA-0015 series, as reported by Whicker and Fehlner (1958) and Gregory (1973).

Table 11 Different cases for CFD simulation in regular head waves

Case No.	Wave/vessel length $\left(\frac{\lambda_w}{L}\right)$	Wave steepness $\left(\frac{h_w}{\lambda_w}\right)$	Wave frequency (ω) (rad/s)	Dimensionless wave frequency $\left(\omega^* = \omega\sqrt{L/g}\right)$
1	0.85	0.0436	5.6	2.72
2	1	0.0370	5.16	2.50
3	1.4	0.02s65	4.36	2.12
4	1.8	0.0206	3.84	1.87
5	2	0.0185	3.65	1.77
6	2.19	0.0169	3.49	1.70
7	2.4	0.0154	3.33	1.62
8	3	0.0123	2.98	1.44
9	4.5	0.0082	2.43	1.18
10	6.5	0.0057	2.02	0.98
11	9	0.0041	1.72	0.83

Before obtaining the heave and pitch motions of the model, a wave elevation calibration test was performed by a wave probe, which was located between the inlet face and the model in the computational domain. The time series of the elevation of generated and sinusoidal waves with the same encounter frequency were compared (Figure 11). A slight phase delay was observed between the generated and sinusoidal waves. The difference in the amplitude between the generated and sinusoidal waves was about 1.86%, which indicates that the grid cell size and time step utilized are reasonable for the current simulation model (Tezdogan et al. 2015).

Figure 12 illustrates the comparison of numerical results and experimental data. The origin of the slight phase delay between the present results and experimental data (in all plots) was due to an error in the generated wave by the numerical method.

Table 10 shows the maximum value of the heave and pitch motion reduction of the vessel equipped with stabilizing fins compared with the bare-hull case. The results showed that the best condition for reducing the heave motion was at an aft fin angle of 10°, whereas the best condition for reducing the pitch motion was at an aft fin of 15°. Thus, fixed stabilizing fins are practical tools for reducing vertical motions.

The heave, pitch, and vertical acceleration RAO diagrams of the semi-SWATH bare-hull model in regular head wave conditions with constant height $h_w = 0.0857$ m at Froude numbers ranging from 0 to 0.51 were obtained based on the cases mentioned in Table 11. The corresponding equations in dimensionless forms of RAO are given below:

$$\begin{aligned} \mathrm{RAO}_{\mathrm{heave}} &= \frac{Z_a}{\zeta_a} \\ \mathrm{RAO}_{\mathrm{pitch}} &= \frac{\theta_a}{k\zeta_a} \\ \mathrm{RAO}_{\mathrm{acc}} &= \frac{aL}{g\zeta_a} \end{aligned} \tag{13}$$

where Z_a is the amplitude of heave motion, $\zeta_a = h_w/2$ is the wave amplitude, θ_a is the amplitude of pitch motion, k is the wavenumber, a is the vertical acceleration at the center of gravity (CG) or bow, and g is the gravitational acceleration.

Figure 13 shows the heave and pitch RAO diagrams versus the dimensionless wavelength (λ_w/L) at four different Froude numbers.

Using Figure 13, the following results were obtained:

1) As the speed increased, the level of heave RAO increased, whereas the level of pitch RAO increased first and then decreased at $Fr > 0.17$.
2) At $Fr = 0.34$, 0.51, a double-peak trend was found for the pitch RAO of the vessel. At both Froude numbers, the first pitch motion peak displayed lower and nearly appears in the proximity of $\lambda_w/L = 2$ ($\omega^* \cong 1.77$). The second peak had a higher value and occurred in the range [4.5–6.5] of the dimensionless wavelength ($0.98 \le \omega^* \le 1.18$). In general, the presence of the peaks can be due to the resonance caused by the coupling of heave and pitch motions.
3) At $Fr = 0.34$, at a dimensionless wavelength of about $\lambda_w/L \cong 2.19$ (in frequency about $\omega^* \cong 1.70$), when the heave RAO reached its peak, the pitch RAO was at its minimum value close to 0. This event occurred when the vessel was periodically at the crest or trough of the incoming waves. In this interesting phenomenon, which can be called "pitch cancelation," almost no moment is applied to the semi-SWATH vessel.

Figure 14 shows the vertical accelerations at CG and bow in the dimensionless form of the RAO diagram at different Froude numbers. In general, increasing the speed can have two effects on the vertical acceleration responses.

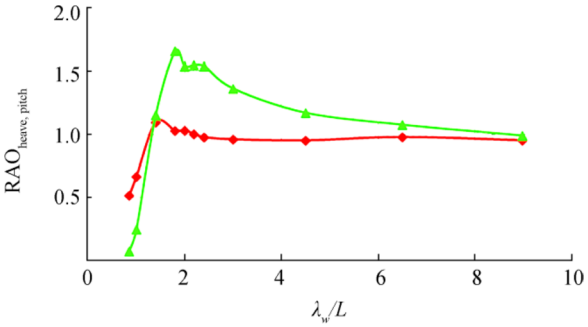

(a) $Fr = 0$

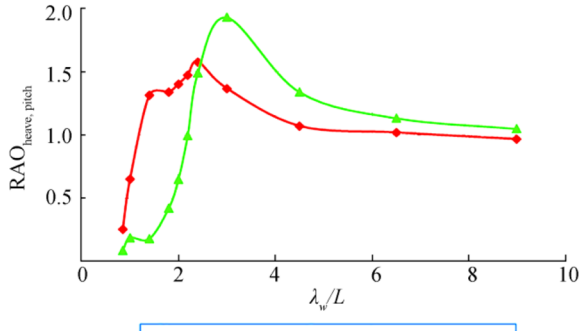

(b) $Fr = 0.17$

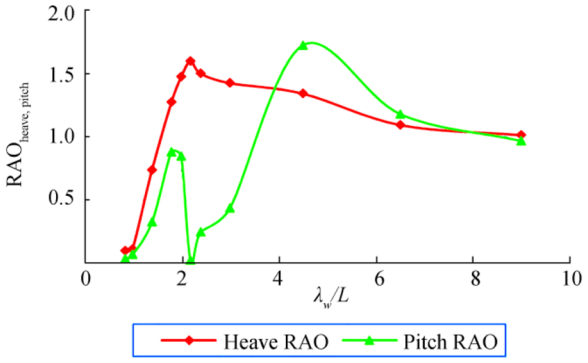

(c) $Fr = 0.34$

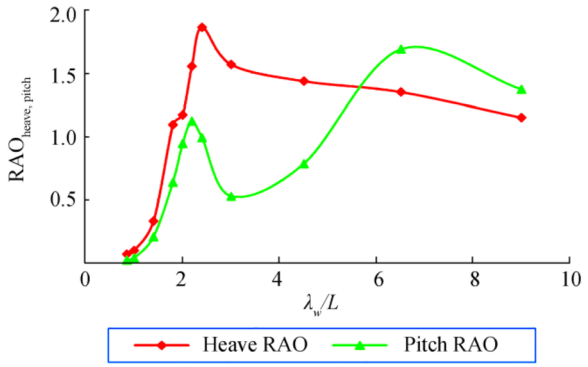

(d) $Fr = 0.51$

Figure 13 Heave and pitch RAO diagrams (for bare-hull case)

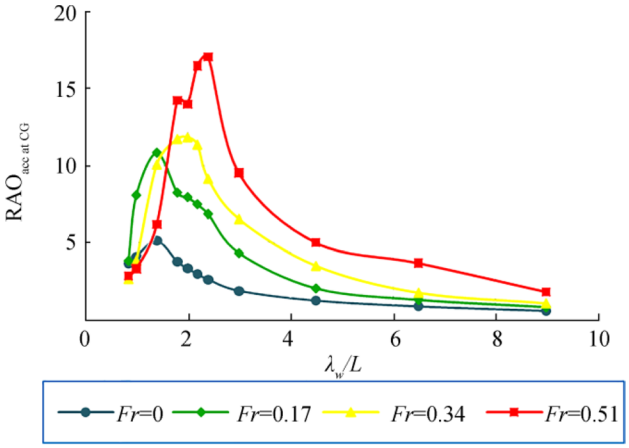

(a) Comparison of CG accelerations

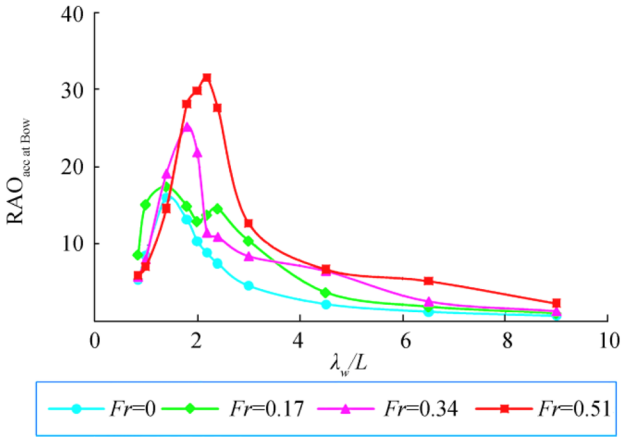

(b) Comparison of bow accelerations

Figure 14 Vertical acceleration RAO diagrams at different Froude numbers

First, the maximum vertical acceleration will increase with speed for the constant wavelength (at a wavelength of about $\lambda_w/L > 1.4$), and secondary the resonance frequency will be at long wavelengths for higher speeds.

5 Conclusion Remarks

The numerical simulation of an advanced semi-SWATH hull in calm water and regular head wave has been done, and the effectiveness of fixed stabilization fins for control and reduction of SWATH vertical motion has also been evaluated. The numerical results also compared with available experimental data, and as a result, the following conclusions can be obtained:

1) By comparing the numerical results and already published experimental data, the CFD numerical method has acceptable accuracy for the prediction of vertical motions of semi-SWATH hulls.
2) Double-peaked RAO were found for pitch motion at $Fr = 0.34$, 0.51. The appearance of the peaks may be due to the resonance phenomenon caused by heave and pitch coupling.
3) When the semi-SWATH vessel was subjected to incoming waves with a length of about $2.19R$ and the vessel length at $Fr = 0.34$, almost no moment was imposed on it. This interesting phenomenon in which only heaving motion is present can be called "pitch cancelation."
4) Based on the presented results, fixed stabilizing fins can also be used for vertical motion reduction of semi-SWATH vessels under head wave conditions.
5) For future research, the calculation of hydrodynamic coefficients of the semi-SWATH vessel using CFD methods and the development of mathematical models for the assessment of the efficiency of active stabilizing fins by modern optimal control theory is intended.

Abbreviations and Nomenclature a_{CG}: Vertical acceleration at the Centre of gravity (m/s^2); B: Half beam of the vessel (m); BEM: Boundary Element Method; CFD: Computational fluid dynamics; CFL: Courant-Friedrichs-Lewy number; CG: Center of Gravity; C_f: Friction coefficient; C_T: Total resistance coefficient; C_W: Wave resistance coefficient; DFBI: Dynamic Fluid Body Interaction; Fr: Froude number $\left(V/\sqrt{gL}\right)$; g: Acceleration due to gravity (m/s^2); GCI: Grid Convergence Index; HRIC: High-Resolution Interface Capture; h_w: Wave height (m); ITTC: International Towing Tank Conference; k: Wave number (rad/m); L: Length between perpendiculars of the hull (m); MII: Motion-Induced Interruptions (1/min); MSI: Motion-Seasickness Incidence (%); RAO: Response Amplitude Operators; R&D: Research and Development; SWATH: Small Waterplane Area Twin Hull; T: Draft of the vessel (m); T_e: Wave encounter period (1/s); Δt: Time step (s); U: Flow velocity (m/s); u^*: Friction velocity (m/s); URANSE: Unsteady Reynolds-Averaged Navier-Stokes Equation; V: Speed of the vessel (m/s); v: Kinematic viscosity (m^2/s); w/wo: With or without; Δx: Cell size dimension (m); y: Absolute distance from the nearest wall (m); $y+$: Dimensionless wall distance (u^*y/v); Z_a: Heave motion amplitude (m); α: Volume fraction of water; β: Viscous interference factor; $(1+K)$: Form factor; ζ_a: Wave amplitude (m); θ_a: Pitch motion amplitude (°); λ_w: Wave length (m); ρ: Density of water (kg/m^3); τ: Wave resistance coefficient interference factor; ω: Wave frequency (rad/s); ω^*: Dimensionless wave frequency $\left(\omega\sqrt{L/g}\right)$; ∇: Volume of displacement (m^3)

References

Ali A, Maimun A, Ahmed YM (2014) CFD application in resistance analysis for advanced semi-SWATH vehicle. Appl Mech Mater 465-466:44–49. https://doi.org/10.4028/www.scientific.net/AMM.465-466.44

Ali A, Maimun A, Ahmed YM, Rahimuddin R, Ghani MPA (2015) Experimental analysis on flow around fin assisted semi-SWATH. Jurnal Teknologi 74(5):91–95. https://doi.org/10.11113/jt.v74.4647

Begovic E, Bertorello C, Mancini S (2015) Hydrodynamic performances of small size swath craft. Brodogradnja 66(4):1–22

Begovic E, Bertorello C, Bove A, De Luca F (2019) Experimental study on hydrodynamic performance of SWATH vessels in calm water and in head waves. Appl Ocean Res 85:88–106. https://doi.org/10.1016/j.apor.2018.10.012

Bonfiglio L, Perdikaris P, Vernengo G, de Medeiros JS, Karniadakis G (2018) Improving SWATH seakeeping performance using multi-fidelity Gaussian process and Bayesian optimization. J Ship Res 62(4):223–240. https://doi.org/10.5957/JOSR.11170069

Brizzolara S, Vernengo G (2011) Automatic computer driven optimization of innovative hull forms for marine vehicles. 10th WSEAS International Conference on Applied Computer and Applied Computational Science, ACACOS'11, Venice, 273-278

Brizzolara S, Vernengo G, Bonfiglio L, Bruzzone D (2015) Comparative performance of optimum high-speed SWATH and semi-SWATH in calm water and in waves. Transact - Soc Naval Arch Mar Eng 123(M):273–286

Bruzzone D (1994) Numerical evaluation of the steady free surface waves. CFD Workshop Ship Res Inst Tokyo I:126–134

Bruzzone D (2003) Application of a Rankine source method to the evaluation of motions of high-speed marine vehicles. Proceedings of the 8th International Marine Design Conference, Athens, Greece, II, 69-79

Campana EF, Peri D (2000) Hydrodynamic performance comparison between twin hulls. International Conference on Ship and Shipping Research, Venice, Italy, P2000-9 Proceedings

Celik IB, Ghia U, Roache PJ, Freitas CJ, Coleman H, Raad PE (2008) Procedure for estimation and reporting of uncertainty due to discretization in CFD applications. J Fluids Eng Trans ASME 130:078001-1–078001-4

Chan HS (1993) Prediction of motion and wave loads of twin-hull ships. Mar Struct 6(1):75–102. https://doi.org/10.1016/0951-8339(93)90010-Z

Cucinotta F, Guglielmino E, Sfravara F, Strasser C (2018) Numerical and experimental investigation of a planing Air Cavity Ship and its air layer evolution. Ocean Eng 152:130–144. https://doi.org/10.1016/j.oceaneng.2018.01.071

De Luca F, Mancini S, Miranda S, Pensa C (2016) An extended verification and validation study of CFD simulations for planing hulls. J Ship Res 60(2):101–118. https://doi.org/10.5957/JOSR.60.2.160010

Dubrovsky V, Lyakhovitsky A (2001) Multi-hull ships. Backbone Publishing Co., Fair Lawn, USA, p 495

Dubrovsky V, Matveev K, Sutulo S (2007) Small water-plane area ships. Backbone Publishing Co., Hoboken, USA, 256

Ferziger JH, Perić M (2002) Computational methods for fluid dynamics. Springer, Berlin, Germany, pp 292–294. https://doi.org/10.1007/978-3-642-56026-2

Frisk D, Tegehall L (2015) Prediction of high-speed planing hull resistance and running attitude. A numerical study using computational fluid dynamics. Master of Science. Department of Shipping and Marine Technology Chalmers University of Technology, Gothenburg, pp 1–51

Gregory DL (1973) Force and moment characteristics of six high-speed rudders for use on high-performance craft. Report 4150, United State Naval Academy, 1-8

Gupta SK, Schmidt TW (1986) Developments in swath technology. Nav Eng J 98(3):171–188. https://doi.org/10.1111/j.1559-3584.1986.tb03428.x

Guttenplan A (2007) Hydrodynamic evaluation of high-speed semi-SWATH vessels. PhD thesis. Massachusetts Institute of Technology, Cambridge, USA, pp 58–60

ITTC (2011) Practical Guidelines for Ship CFD Applications - 7.5-03-02-03. 26th International Towing Tank Conference, Rio De Jenerio, Brazil

ITTC QM (2002) Uncertainty analysis in CFD verification and validation methodology and procedures- 7.5-03-01-01. Proceedings of the 23rd International Towing Tank Conference, Venice, Italy

Jupp M, Sime R, Dudson E (2014) Xss-a next generation windfarm support vessel. RINA Conference: Design & Operation of Wind Farm Support Vessels, London, 29-30

Kahramanoğlu E, Çakıcı F, Doğrul A (2020) Numerical prediction of the vertical responses of planing hulls in regular head waves. J Mar Sci Eng 8(6):455. https://doi.org/10.3390/jmse8060455

Kallio JA (1976) Seaworthiness characteristics of a 2900 tons small waterplane area twin hull (SWATH). David W. Taylor Naval Ship Research and Development Center, Ship Performance Department, SPD-620-03, Maryland

Pérez-Arribas F, Calderon-Sanchez J (2020) A parametric methodology for the preliminary design of SWATH hulls. Ocean Eng 197:106823. https://doi.org/10.1016/j.oceaneng.2019

Salvesen N, Von Kerczek CH, Scragg CA (1985) Hydro-numeric design of swath ships. Transact - Soc Naval Arch Mar Eng:325–346

Siemens PLM (2019) STAR-CCM+ User Guide Version 13.04. Siemens PLM. Software Inc, Munich, Germany

Stern F, Wilson R, Shao J (2006) Quantitative V&V of CFD simulations and certification of CFD codes. Int J Numer Methods Fluids 50(11):1335–1355. https://doi.org/10.1002/fld.1090

Sun H, Jing F, Jiang Y, Zou J, Zhuang J, Ma W (2016) Motion prediction of catamaran with a semisubmersible bow in wave. Polish Maritime Research 23(1):37–44. https://doi.org/10.1515/pomr-2016-0006

Tezdogan T, Demirel YK, Kellett P, Khorasanchi M, Incecik A, Turan O (2015) Full-scale unsteady RANS CFD simulations of ship behaviour and performance in head seas due to slow steaming. Ocean Eng 97:186–206. https://doi.org/10.1016/j.oceaneng.2015.01.011

Vernengo G, Brizzolara S (2017) Numerical investigation on the hydrodynamic performance of fast SWATHs with optimum canted struts arrangements. Appl Ocean Res 63:76–89. https://doi.org/10.1016/j.apor.2017.01.009

Vernengo G, Bruzzone D (2016) Resistance and seakeeping numerical performance analyses of a semi-small waterplane area twin hull at medium to high speeds. J Mar Sci Appl 15(1):1–7. https://doi.org/10.1007/s11804-016-1343-0

Vernengo G, Apollonio CM, Bruzzone D, Bonfiglio L, Brizzolara S (2018) Hydrodynamics performance of high-speed multi-hulls in waves. Marit Transport Harvest Sea Resourc 1(1996):493–500

Voxakis P (2012) Ship hull resistance calculations using CFD methods. PhD thesis. Massachusetts Institute of Technology, Cambridge, USA, pp 24–30

Wang C, Lin Y, Hu Z, Geng L, Li D (2016) Hydrodynamic analysis of a SWATH planing USV based on CFD. OCEANS 2016, Shanghai, 2-5. https://doi.org/10.1109/OCEANSAP.2016.7485460

Whicker LF, Fehlner LF (1958) Free-stream characteristics of a family of low aspect ratio all movable control surfaces for application to ship design. In: Report: AD-A014 272. David Taylor Model Basin, Washington, D.C.

Wilson RV, Stern F, Coleman HW, Paterson EG (2001) Comprehensive approach to verification and validation of CFD simulations—part 2: application for rans simulation of a cargo/container ship. J Fluids Eng Transact ASME 123(4):803–810. https://doi.org/10.1115/1.1412236

Yaakob OB, Mekanikal FK (2006) Development of a semi-SWATH craft for Malaysian waters. University of technology, Malaysia

Yun L, Bliault A, Rong HZ (2018) High speed catamarans and multihulls: technology, performance, and applications. Springer 246-249. https://doi.org/10.1007/978-1-4939-7891-5